
ORIGINAL ARTICLE

Journal Section

Spectral scaling of unstably-stratified atmospheric flows: understanding the low frequency spread of Kaimal model

Claudine Charrondière^{1*} | Ivana Stiperski^{1*}

¹Department of Atmospheric and Cryospheric Sciences, University of Innsbruck, Innsbruck, Austria

Correspondence

Ivana Stiperski,
Department of Atmospheric and Cryospheric Sciences,
University of Innsbruck, Innrain 52f,
Innsbruck, Austria
Email: ivana.stiperski@uibk.ac.at

Funding information

These results are part of a project that has received funding from the European Research Council (ERC) under the European Union's Horizon 2020 research and innovation programme (Grant agreement No. 101001691).

For more than five decades, a notable spread in the low frequencies of velocity and temperature spectra, scaled using inertial subrange properties and Monin-Obukhov similarity theory, has been observed in unstable stratification. A large ensemble of 14 datasets, over relatively simple terrain (from flat and homogeneous to gentle slope or valley floor) and very complex terrain (steep slope, crater rim, mountain top), are used to assess the reasons of this low-frequency behaviour.

Turbulence anisotropy is shown to be the primary factor influencing the spectral energy at the largest scales and the spectral peak position of streamwise and spanwise velocity spectra, with stability acting as a secondary factor. On the contrary, the low-frequency behaviour of surface-normal and temperature spectra is dominated by stability effects, while turbulence anisotropy plays a secondary role. These observations are valid over both simple and complex terrain, even though variability of the largest scales of complex terrain datasets integrate other processes not included in turbulence anisotropy or stability conditions.

Using a combination of non-dimensional turbulence parameters - temperature and velocity variances as well as

Abbreviations: MOST, Monin-Obukhov similarity theory; ML, Mixed Layer; TKE, Turbulence Kinetic Energy.

* Equally contributing authors.

dissipation of turbulence kinetic energy and of temperature variance - and of a semi-empirical model provided in the literature, we are able to describe the behaviour of the velocity and temperature spectra with only turbulence anisotropy and stability as input parameters.

Finally, the paper provides some insights into the nature of anisotropic eddies, as well as the relationship between the boundary layer height and the spectral behaviour.

KEYWORDS

Atmospheric Boundary Layer, Complex Terrain, Monin-Obukhov Similarity Theory, Surface Layer, Turbulence Anisotropy

1 | INTRODUCTION

Spatial structure of atmospheric boundary layer is tightly coupled to the spectral characteristics of turbulence (Tennekes and Lumley, 1972). Turbulence spectra, thus, provide invaluable information on the nature and structure of atmospheric turbulence, in particular on how energy (or variance) is distributed among the different scales of motions and how these scales interact with each others. In fact, spectral analysis is widely used in studying atmospheric boundary layer flows, especially in terms of understanding the process of turbulence cascade (e.g., Kolmogorov, 1941a,b; Stiperski et al., 2021b), the size and structure of most energetic eddies (e.g., Salesky and Anderson, 2018; Stiperski et al., 2020, 2021a; Sun et al., 2020; Lan et al., 2022), the departure of complex flows from canonical conditions (e.g., Rotach, 1995; Villani et al., 2003; Chamecki and Dias, 2004; Babić and Rotach, 2018), the impact of large-scales atmospheric motions on the local flow (Dupont and Patton, 2022), in testing the numerical schemes of weather prediction models and large eddy simulations (e.g., Sukoriansky et al., 2005; Wilczek et al., 2015; Gibbs and Fedorovich, 2014; Dairay et al., 2017), as well as in providing a theoretical framework for widely used similarity scaling relations (e.g., Gioia et al., 2010; Katul et al., 2011, 2013, 2014; Banerjee et al., 2015; Li, 2021).

Surface-layer turbulence spectra are also one of the turbulence statistics that follow the Monin-Obukhov similarity theory (MOST, Monin and Obukhov, 1954). The first and still most widely used spectral scaling framework was proposed by Kaimal et al. (1972), who suggested scaling relations for the spectra of velocity and temperature, as well as co-spectra of momentum and sensible heat fluxes. The spectral scaling was based on the Kolmogorov's hypothesis (Kolmogorov, 1941b) such that the high-frequency part of the scaled spectra collapse in the inertial subrange, allowing a study of the low-frequency part of the spectra under MOST. Using data from the Kansas field experiment over horizontally homogeneous and flat terrain (Haugen et al., 1971), Kaimal et al. (1972) showed that under stable stratification the spectral energy at low frequencies is driven by MOST stability parameter $\zeta = z/L$, where z is the height above the surface and L the Obukhov length, defined as (Stull, 1988):

$$L = -\frac{\bar{\theta}}{\kappa g} \frac{u_*^2}{T_*}. \quad (1)$$

Here, $\bar{\theta}$ is the mean potential temperature, $g = 9.81 \text{ m s}^{-2}$ is the effective gravity, $\kappa = 0.4$ is the von Kármán constant, $u_* = (\overline{u'w'^2} + \overline{v'w'^2})^{1/4}$ is the friction velocity and $T_* = -\overline{w'\theta'}/u_*$ is the temperature scale, where $\overline{w'\theta'}$ is the kinematic

sensible heat flux, while $\overline{u'w'}$ and $\overline{v'w'}$ are the momentum fluxes.

Still, in unstable conditions, Kaimal et al. (1972) observed a large spread of the low-frequency data that did not follow a particular scaling, concluding that the spectra "tend to cluster in a random fashion". They only noted a small separation of the surface-normal velocity spectra linked to ζ when approaching neutral conditions, and offered no hypothesis to explain such a spread. Later, Olesen et al. (1984) used an analytical model based on the same approach to derive scaling laws for the velocity spectra both in the low-frequency and high-frequency range, but also failed in predicting the behaviour of low-frequency spectral energy for horizontal velocity spectra in unstable conditions. Given that the integral of the spectrum yields the variance, the non-scaling of the low-frequency part of the horizontal velocity spectra in unstable stratification can be linked to the failure of MOST in explaining the scaling of horizontal velocity variances, even over flat terrain (e.g., Wyngaard and Coté, 1974; Kader and Yaglom, 1990).

Some refinements of MOST have been developed since. A mixed layer scaling approach of Panofsky et al. (1977) recognised that the horizontal velocity variances are driven by inactive large-convective eddies, and thus that the mixed layer (ML) depth z_i and not the measurement height should be the relevant scaling height. McNaughton et al. (2007) extended this approach to spectra and co-spectra. For temperature spectra and heat flux co-spectra, the scaling was then improved by a combination of z_i and the surface friction layer height (Laubach and McNaughton, 2009) and explains the position and spectral density of the energy peak. This means that the spectral shape and density are related to both local (Kaimal et al., 1972) and bulk (Laubach and McNaughton, 2009) information. Based on the fact that the flow is influenced both by buoyancy and shear in the majority of stability conditions (except highly convective/stable), Tong and Nguyen (2015) developed the Multi-Point Monin-Obukhov theory, where the Obukhov length serves not only as the vertical, but also as the horizontal length scale. Through their approach, they could explain the commonly observed spectral slopes.

Recently, Stiperski and Calaf (2018), Stiperski et al. (2019) and Stiperski and Calaf (2023) showed that bulk turbulence statistics, such as velocity variances, temperature variance and turbulence kinetic energy (TKE) dissipation rate can be reconciled under MOST if turbulence anisotropy is included as an additional scaling parameter. Mosso et al. (2023) extended the analysis to scaled velocity and temperature gradients and obtained similar conclusion and scaling relations. The novel scaling relations drastically improve scaling and allow it to be extended to complex terrain, where the basic assumptions of MOST (horizontally homogeneous and flat terrain, constant vertical flux profile, no subsidence) are clearly violated. Stiperski and Calaf (2023) suggested that, for horizontal velocity variances, the scaling based on anisotropy outperforms the ML scaling of Panofsky et al. (1977), which implies that turbulence anisotropy incorporates the majority of the information on the boundary conditions driving the flows (including the ML height). Given the difficulties of obtaining ML height from conventional turbulence measurements and the lack of routine boundary layer height observations, the aforementioned scaling proposed in McNaughton et al. (2007) or in Laubach and McNaughton (2009) are not easy to apply. A local parameter such as turbulence anisotropy is thus preferred for understanding spectral behaviour. At the same time, spectral analysis can help shed more light on the nature of turbulence anisotropy and how it is impacted by terrain complexity.

Here we explore whether new results of Stiperski and Calaf (2023) can be extended to two-point statistics such as spectral scaling of Kaimal et al. (1972), in order to explain the spread of the low frequency range of velocity and temperature spectra in unstable stratification. More specifically, we investigate the influence of turbulence anisotropy on the spectral density and the location of the spectral peak for datasets with varying degree of complexity. We first focus on canonical conditions where the influence of terrain is expected to be small, and then proceed to complex mountainous conditions to show how much our method can account for the complexity of turbulence. Finally we explore turbulence anisotropy in light of the newly developed spectral scaling.

Section 2 focuses on describing the theoretical framework on which the paper is based. Section 3 provides an overview of the 14 datasets used, as well as a description of the data processing. Section 4 presents the results with a special focus on the influence of stability conditions and turbulence anisotropy (Section 4.1 and 4.2), separation between turbulence anisotropy and atmospheric stability effects (Section 4.3), analytical modeling (Section 4.4), and the influence of mountainous terrain (Section 4.5), followed by a discussion on the contribution of the mixed layer height to spectral scaling in Section 5 and conclusions in Section 6.

2 | THEORETICAL FRAMEWORK

The spectral scaling proposed by Kaimal et al. (1972) rests on two scaling frameworks: the inertial subrange scaling as proposed by Kolmogorov (1941a) and Kolmogorov (1941b), and similarity functions of MOST (Monin and Obukhov, 1954). Given the observed non-constancy of fluxes with height in non-canonical conditions (e.g., Nadeau et al., 2013; Sfyri et al., 2018), we use the local scaling approach (Nieuwstadt, 1984; Stiperski and Calaf, 2023) and scale the spectra at each measurement level with the respective fluxes at that level. Note that the classic MOST is an asymptotic case of local scaling in conditions when fluxes are constant with height.

According to Kolmogorov's hypotheses (Kolmogorov, 1941a,b), the spectral density of the velocity spectra S_{u_i} (with $u_1 = u$, $u_2 = v$ and $u_3 = w$ for streamwise, spanwise and surface-normal velocity components respectively) and temperature spectra S_θ in the inertial subrange are solely determined by the dissipation rates of TKE ε and of half the temperature variance N_θ respectively, and can be written as (Pope, 2000; Wyngaard, 2010):

$$S_{u_i}(k_x) = A_i \varepsilon^{2/3} k_x^{-5/3}, \quad (2)$$

$$S_\theta(k_x) = A_\theta N_\theta \varepsilon^{-1/3} k_x^{-5/3}. \quad (3)$$

The wavenumber k_x is parallel to the mean flow direction, A_i is the Kolmogorov constant, equal to $A_1 \approx 0.55$ and $A_2 = A_3 = \frac{4}{3} A_1$ for the three velocity components, and $A_\theta \approx 0.8$ is the Obukhov-Corrsin constant for the temperature variance. Following the Taylor's frozen turbulence hypothesis (Taylor, 1938), the wavenumber spectrum can be converted from spatial to temporal domain, $k_x S(k_x) = f S(f)$, such that $k_x = 2\pi f / \bar{u}$, where f is the frequency and \bar{u} is the mean wind speed (Wyngaard, 2010). Finally, following MOST, the spectra can be written in their scaled form as (Kaimal et al., 1972):

$$\frac{f S_{u_i}(f)}{u_*^2} = a_i \phi_\varepsilon^{2/3} n^{-2/3}, \quad (4)$$

$$\frac{f S_\theta(f)}{T_*^2} = a_\theta \phi_N \phi_\varepsilon^{-1/3} n^{-2/3}. \quad (5)$$

Here the spectra are scaled based on the key surface-layer parameters: z , u_* and T_* . The scaled frequency $n = fz / \bar{u}$ and new values for the constants are $a_i = A_i (2\pi\kappa)^{-2/3}$, which gives $a_1 \approx 0.3$, $a_2 = a_3 \approx 0.4$, and similarly $a_\theta \approx 0.43$. Finally, the MOST relations for TKE dissipation rate ϕ_ε and for half the temperature variance ϕ_N are defined as:

$$\phi_\varepsilon = \frac{\kappa z \varepsilon}{u_*^3}, \quad (6)$$

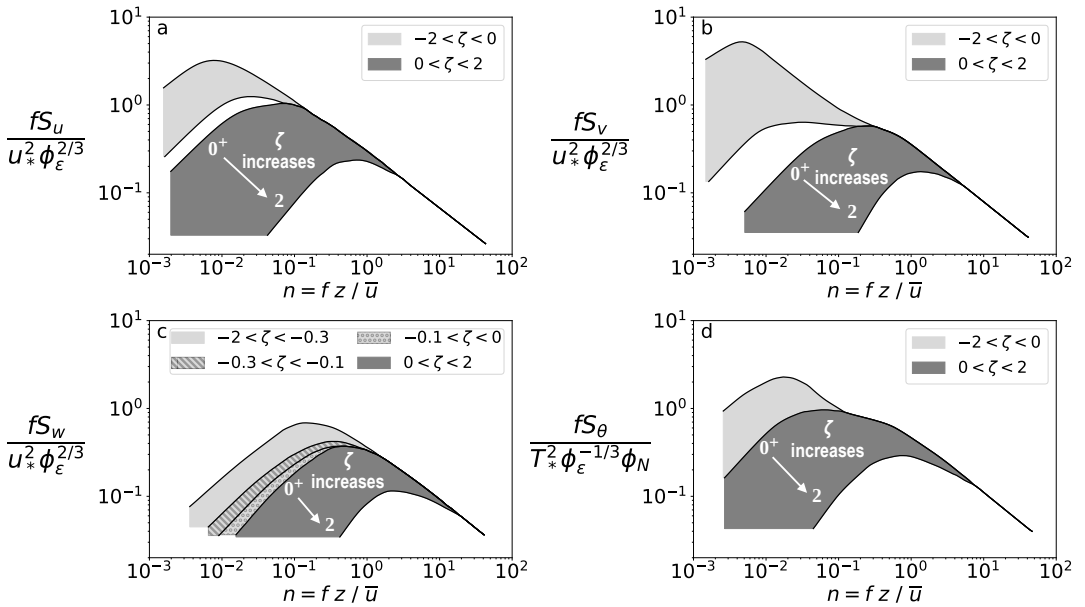


FIGURE 1 Scaled surface layer spectra for (a) streamwise, (b) spanwise, and (c) surface-normal velocity, and (d) temperature, as a function of stability parameter ζ . Dark gray represents stable conditions, and light gray is for unstable conditions. Figure adapted from Kaimal and Finnigan (1994).

$$\phi_N = \frac{\kappa z N_\theta}{u_* T_*^2}. \quad (7)$$

The scaled spectra based on Eqs. 4 and 5 collapse in the inertial subrange (Fig. 1).

Kaimal et al. (1972) observed that the low frequency ranges of both velocity and temperature spectra vary according to the stability parameter for stable conditions ($\zeta > 0$): the more stable the atmosphere, the less low frequency energy is present in the scaled spectra, and the spectral peak is found at higher n , such that energy containing eddies decrease in size and energy content as stratification increases. However, for $\zeta < 0$, no such trend could be inferred. The only apparent separation between spectra according to ζ in unstable conditions could be discerned for surface-normal velocity in close to neutral stratification $-0.3 \leq \zeta \leq 0$ (Fig. 1c).

To derive a universal model for the spectra in stable conditions, Kaimal et al. (1972) studied the link between the scaled frequency of the spectral peak n_m and ζ . Using $n_m = f(\zeta)$, the spectra can then be described by a universal shape for stable atmospheric conditions. However, for horizontal velocity components in unstable atmospheric conditions, there is no clear trend of n_m according to ζ . Some studies took a constant n_m (e.g., Kaimal, 1973; Caughey, 1977), but the low-frequency spectral density of unstable horizontal velocity components was then not captured. This approach was employed later by Olesen et al. (1984), who successfully reproduced spectra from the Kansas experiment in the stable conditions using n_m proportional to the scaled velocity gradient ϕ_m , taking the MOST relations for ϕ_m and ϕ_ε . In unstable conditions, Olesen et al. (1984) assumed that $n_m = f(\zeta)$ only for small values of ζ , and that it rapidly tends to a constant when stratification approaches the free convective limit. This reasoning is able to explain the behaviour shown in Kaimal et al. (1972) for surface-normal velocity spectra.

According to Olesen et al. (1984), the scaled velocity spectra assume the following expression:

$$\frac{f S_{u_i}(f)}{u_*^2} = \frac{A_{u_i} n^\gamma}{(1 + B_{u_i} n^\alpha)^\beta}, \quad (8)$$

where parameters A_{u_i} and B_{u_i} determine the position of the spectra on the ordinate, while α , β and γ influence its shape by providing asymptotic behaviour both at low and high frequencies. Following Eq. 4, the inertial subrange asymptote ($n \gg 1$) of Olesen's model, as described in Eq. 8, imposes two conditions on the free parameters:

$$\gamma - \alpha\beta = -2/3, \quad (9)$$

$$A_{u_i} = a_i \phi_\varepsilon^{2/3} B_{u_i}^\beta. \quad (10)$$

Integrating Eq. 8 over the entire frequency range, Olesen et al. (1984) also derived an expression for the scaled velocity variance ϕ_{u_i} , which, when combined with Eq. 10, provides an analytical solution for B_{u_i} :

$$B_{u_i} = \left(C_{u_i} \frac{\phi_{u_i}^2}{\phi_\varepsilon^{2/3}} \right)^P \text{ with } C_{u_i} = \frac{\alpha}{a_i} \frac{\Gamma(\beta)}{\Gamma\left(\frac{\gamma}{\alpha}\right) \Gamma\left(\frac{2}{3\alpha}\right)} \text{ and } P = \frac{\alpha}{\alpha\beta - 1}, \quad (11)$$

where Γ is the gamma function, and the scaled velocity variance is defined as:

$$\phi_{u_i}^2 = \frac{\sigma_{u_i}^2}{u_*^2}. \quad (12)$$

Equation 11, combined with Eq. 10, allowed to compute the parameters A_{u_i} and B_{u_i} , provided a set of values for α , β and γ . This approach has been used for example in Tieleman (1995), and has the advantage of not requiring any information regarding the position of the maximum spectral energy n_m . Tieleman (1995) described the mathematical shapes of A_{u_i} and B_{u_i} for three sets of (α, β, γ) , and showed analytically that the velocity spectra are a function of ϕ_{u_i} only. Note that he used $\phi_\varepsilon = 1$, which is a good approximation only for near-neutral conditions. We thus do not expect this solution to perform well in convective conditions.

Provided that $\phi_\varepsilon \neq 1$ in the range of stability considered in the present study (down to $\zeta = -100$) we use the following adaptation of Eq. 8:

$$\frac{f S_{u_i}(f)}{u_*^2 \phi_\varepsilon^{2/3}} = \frac{a_i B_{u_i}^\beta n^\gamma}{(1 + B_{u_i} n^\alpha)^\beta} \quad (13)$$

One could adapt this semi-empirical model to temperature spectra consistently with Eq. 5:

$$\frac{f S_\theta(f)}{T_*^2 \phi_\varepsilon^{-1/3} \phi_N} = \frac{a_\theta B_\theta^\beta n^\gamma}{(1 + B_\theta n^\alpha)^\beta}, \quad (14)$$

$$\text{where } B_\theta = \left(C_\theta \frac{\phi_\theta^2}{\phi_\varepsilon^{-1/3} \phi_N} \right)^P, \quad (15)$$

TABLE 1 Similarity scaling functions in the framework of MOST and according to the new framework of Stiperski and Calaf (2023)

	Monin-Obukhov similarity theory	Stiperski and Calaf (2023)
ϕ_u	$2.55 [1 - 3\zeta]^{1/3}$	$[0.784 - 2.582 \log(y_B)] [1 - 3\zeta]^{1/3}$
ϕ_v	$2.05 [1 - 3\zeta]^{1/3}$	$[0.725 - 2.702 \log(y_B)] [1 - 3\zeta]^{1/3}$
ϕ_w	$1.25 [1 - 3\zeta]^{1/3}$	$[1.119 - 0.019y_B - 0.065y_B^2 + 0.028y_B^3] [1 - 3\zeta]^{1/3}$
ϕ_θ	$0.99 [0.063 - \zeta]^{-1/3}$, when $\zeta < -0.05$ $0.015 \zeta ^{-1} + 1.76$, when $\zeta > -0.05$	$1.07 [0.05 + \zeta]^{-1/3}$ $+ [-1.14 + (0.017 + 0.217y_B) \zeta ^{-9/10}] [1 - \tanh(10 \zeta ^{2/3})]$
ϕ_ε	$[1 - 3\zeta]^{-1} - \zeta$	$a [1 - 3\zeta]^{-1} - \zeta b$ for ε_u : $a = 0.371 + 1.811y_B$ $b = 0.908 + 0.166y_B^{-1} + 0.009y_B^{-2}$ for ε_w : $a = 0.219 + 1.846y_B$ $b = 0.635 + 0.052y_B^{-1} + 0.006y_B^{-2}$
ϕ_N	$0.85 [1 - 6.4\zeta]^{-2/3} / \phi_\varepsilon^{-1/3}$	

C_θ is defined as C_{u_i} in Eq. 11, replacing a_i by a_θ . The scaled temperature variance is defined as:

$$\phi_\theta^2 = \frac{\sigma_\theta^2}{T_*^2}. \quad (16)$$

To include the information on turbulence anisotropy, we follow the work of Stiperski and Calaf (2023) who recently provided new empirical relations for ϕ_{u_i} , ϕ_θ and $\phi_\varepsilon = f(y_B, \zeta)$ that include the degree of anisotropy y_B as a second dimensionless parameter (Table 1). The degree of anisotropy is quantified by the anisotropy invariant analysis of the normalized anisotropy tensor b_{ij} (Lumley, 1978):

$$b_{ij} = \frac{\overline{u'_i u'_j}}{2e} - \frac{1}{3} \delta_{ij}, \quad (17)$$

where $\overline{u'_i u'_j}$ is the Reynolds stress tensor, $e = 0.5\overline{u'_i u'_i}$ is the TKE, and δ_{ij} is the Kronecker delta. The degree of turbulence anisotropy is then quantified through the invariant y_B , determined from the smallest eigenvalue of b_{ij} , namely λ_3 , following Banerjee et al. (2007):

$$y_B = (3\lambda_3 + 1) \frac{\sqrt{3}}{2}. \quad (18)$$

where $y_B = \sqrt{3}/2$ corresponds to pure isotropy, while $y_B = 0$ is the most anisotropic state. For unstable stratification, the invariant x_B was shown not to be important (Stiperski et al., 2019). More details on the anisotropy analysis are provided in Stiperski and Calaf (2018). The new scaling relations for the ϕ functions thus make it possible to include anisotropy into spectral scaling.

3 | DATA

3.1 | Datasets

The 14 datasets used in the present study are summarized in Table 2. These datasets include: Advection Horizontal Array Turbulence Study (AHATS, Horst et al., 2004); Cabauw experimental site for Atmospheric Research (Cesar, Verkaik and Holtslag, 2007); Cooperative Atmosphere Surface Exchange Study 1999 (CASES-99, Poulos et al., 2002); five of the Innsbruck Box (i-Box, Rotach et al., 2017) turbulence towers (CS-VF0, CS-SF1, CS-NF10, CS-NF27, CS-MT21) together with the Im Hinteren Eis station; the NEAR and RIM towers from the Second Meteor Crater Experiment (METCRAX II, stations MC-NEAR and MC-Rim, Lehner et al., 2016); the F2 tower from the Mesoscale Alpine Programme MAP-Riviera experiment (Riviera, Rotach et al., 2004) and the Central and West towers from Terrain-induced Rotor Experiment (T-REX, stations T-RexC and T-RexW, Grubišić et al., 2008).

The stations are separated into two categories. The first category groups datasets that are closest to flat terrain (maximum slope is 3.25°): AHATS, Cabauw, CASES-99, CS-VF0, CS-SF1, MC-Near, T-RexC and T-RexW. We will refer to them as simple terrain thereafter. Note that CS-VF0, T-RexC and T-RexW are on the valley floor, meaning that they are surrounded by mountains even though they are on a relatively flat terrain. The second group is composed of datasets acquired either on steep slopes (from 10° to 40° , CS-NF10, CS-NF27 and Riviera), or in a highly complex configuration such on mountain tops or ridges (CS-MT21, Im Hinteren Eis, MC-Rim). We will refer to them as complex mountainous terrain.

3.2 | Data processing

Turbulence data post-processing follows the procedure described in detail in Stiperski et al. (2019) and used in Stiperski and Calaf (2023). All datasets were double rotated (Aubinet et al., 2012) into the streamline coordinate system where u_1 is the streamwise, u_2 the spanwise, and u_3 the surface-normal velocity component. This coordinate system is standard in complex terrain studies, for which surface-parallel (streamwise and spanwise) direction, will diverge strongly from the horizontal. Turbulence statistics were determined based on the 30-min Reynolds averaging, with prior detrending, given that the present study focuses only on unstable conditions (e.g., Babić et al., 2017; Stiperski and Calaf, 2018). Furthermore, the data were required to be unstable at all measurement levels, and be acquired during daytime to avoid including nighttime counter-gradient fluxes into the statistics.

The following quality control was additionally applied. We kept only stationary data according to the stationarity test of Foken and Wichura (1996), with a threshold of 30%. The stationarity test was applied to the mean wind speed, as well as the sensible heat flux $\overline{w'\theta'}$ (except in near-neutral conditions, $\zeta > -0.05$, where the non-stationarity could be solely due to the small magnitude of the flux) and the turbulent momentum flux $\overline{u'w'}$ (except in highly convective conditions, $\zeta < -1$, where this flux has a small magnitude). Furthermore, we excluded 30-min segments for which the turbulent sensible heat flux $\overline{w'\theta'} < 0.01 \text{ m K s}^{-1}$ at the corresponding measurement height, following De Franceschi et al. (2009) and Nadeau et al. (2013). Such a small flux can be a sign of the (morning/evening) transition regime where $\overline{w'\theta'}$ integrates contributions from both unstable and stable regimes at different scales.

Spectral scaling of Kaimal et al. (1972) requires the knowledge of the TKE dissipation rate ε and the dissipation rate of half the variance N_θ (Eqs. 4 and 5). These dissipation rates were determined from the second order structure function for streamwise, spanwise and surface-normal velocity variances (Chamecki and Dias, 2004) and for temperature variances (Kiely et al., 1996), under the usual assumptions of the existence of the inertial subrange (Kolmogorov,

TABLE 2 Information on turbulence datasets used in the study and site characteristics

Experiment	Station name	Surface type	Terrain complexity Slope angle	Time range available	Measurement heights (m)
AHATS California (USA)	AHATS	Fallow land	Flat	Jun-Aug, 2008	1.55, 3.3, 4.24, 5.53, 7.08, 8.05
Cesar Netherlands	Cabauw	Grass land	Flat	Jul-Oct, 2007	60, 100
CASES-99 Kansas (USA)	CASES-99	Grass land	Flat	Oct, 1999	5, 10, 20, 30, 40, 50, 55
I-Box Tirol (Austria)	CS-VF0	Mixed agricultural	0.5°	Jan-Dec, 2015	4, 8.7, 16.9
	CS-SF1	Alpine meadow	1°	Jan-Dec, 2015	6.6
	CS-NF10	Alpine meadow	10°	Jan-Dec, 2015	6.65
	CS-NF27	Alpine meadow	27°	Oct-May, 2018	1.3, 6.06
	CS-MT21	High alpine vegetation	Mountain top	Apr-Oct, 2015	4.67
Im Hinteren Eis Tirol (Austria)	Im Hinteren Eis	Raw ground / snow	Mountain top	Jun-Oct, 2020	3.3
METCRAX II Arizona (USA)	MC-NEAR	Desert	1°	Oct, 2013	10, 15, 20, 25, 30, 30, 40, 45, 50
	MC-Rim	Desert	Crater rim	Oct, 2013	5, 10, 15, 20, 25, 30, 35, 40
Map-Riviera Switzerland	Riviera	High alpine vegetation	40°	Aug-Sept, 1999	3.1, 11
T-REX California (USA)	T-RexC	Desert	< 0.5°	Mar-Apr, 2006	5, 10, 15, 20, 25, 30
	T-RexW	Desert	3.25°	Feb-Apr, 2006	5, 10, 15, 20, 25, 30

1941a):

$$\varepsilon_{u_i} = \left[\frac{D_{ii}(r)}{C_2^{u_i}} \right]^{3/2} r^{-1}, \quad (19)$$

$$N_\theta = \left[\frac{D_{\theta\theta}(r)}{C_2^\theta} \right] \varepsilon_u^{1/3} r^{-2/3}, \quad (20)$$

where r is the streamwise separation distance, and $C_2^u = 1.97$, $C_2^v = C_2^w = \frac{4}{3}C_u$, and $C_2^\theta = 3.2$. To assure that the second-order structure functions were evaluated within the inertial subrange, only lags for which the slope of the structure functions fell within the range of $2/3 \pm 10\%$ were used.

Since some datasets cover a longer period or contain more measurement levels than others (Table 2), subsampling with replacement was used to build an ensemble of 8 simple-terrain datasets, to ensure that each dataset is equally represented in the analysis. Each dataset within the ensemble was subsampled to have 500 averaging periods within each bin of ζ or y_B . Two ensembles were thus independently created for spectra binned according to the logarithmically spaced ζ and linearly spaced y_B . The complex terrain datasets were evaluated independently. In the following figures, we present the ensemble medians and the interquartile ranges obtained from the bins of the logarithmically spaced normalized frequency n . Each bin of logarithmically spaced n was required to have data from at least three datasets, and more than ten 30-min segments.

4 | RESULTS

4.1 | Effect of stability on the spectra

We first explore the classical scaling of Kaimal et al. (1972) and bin the ensemble data according to ζ (Fig. 2). In agreement with Kaimal (1973), we observe no dependence of the surface-parallel velocity spectra (S_u and S_v) on ζ , and only a small dependence of S_w . We, however, observe three major differences between our and Kaimal (1973)'s results. The low-frequency part of the spanwise spectra S_v show reduced spectral density in the near-neutral conditions ($\zeta > -0.1$) and a plateau-like shape, compared to more unstable stratification. The existence of a plateau (observed also in individual datasets), indicates a continuum of eddy sizes contributing significantly to the total variance. In convective conditions the spectral peak of S_v is better defined, although still broader than in the streamwise velocity spectra S_u . The spanwise velocity spectra S_v also exhibits a slightly concave shape between the frequency of the energy peak and lowest frequency limit of the inertial subrange, especially visible for very anisotropic conditions, as already pointed out in Kaimal (1978).

The small dependence of S_w on ζ stems solely from the dependence of the position of the spectral peak on ζ . This peak is shifted from approximately $n = 0.1$ in very convective conditions to approximately $n = 0.7$ when $|\zeta| < 1$. This means that the surface-normal extent of the most energetic eddies is largest in convective conditions, as expected. However, we do not observe any impact of stability on the lowest frequencies.

The major difference between Kaimal (1973) results and ours arises for temperature spectra, which show a very clear dependence on ζ . An increase of $|\zeta|$ is seen to correspond to a decrease of the low-frequency spectral energy and a shift of the spectral peak towards smaller scales. Laubach and McNaughton (2009) also mentioned such a shift of the peak, with increasing instability during the day.

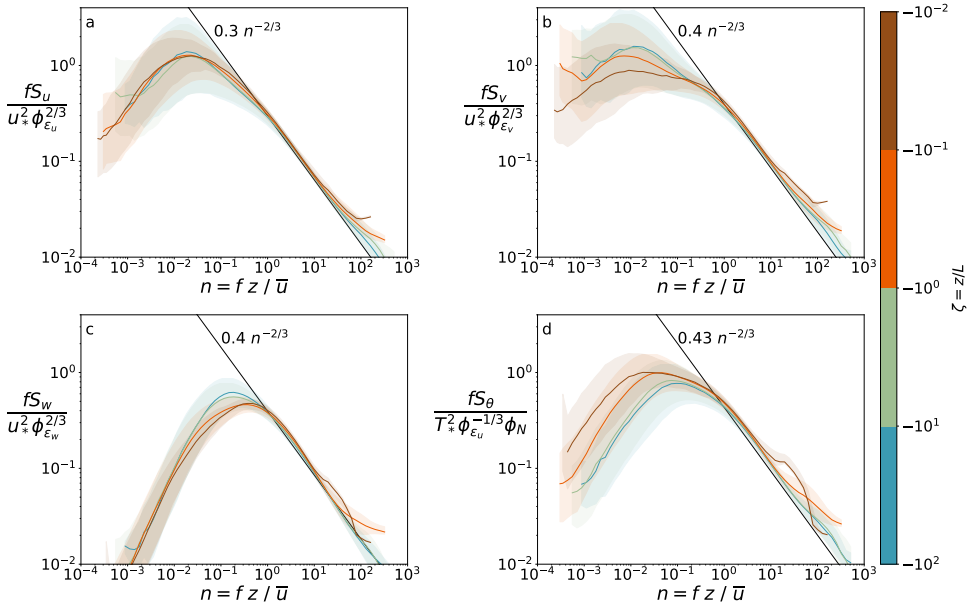


FIGURE 2 Ensemble of simple-terrain spectra of (a) streamwise, (b) spanwise and (c) surface-normal velocity and (d) temperature binned according to the logarithmically spaced stability parameter ζ (colour). Median of each ζ bin is shown with a solid colored line, and the interquartile range in shading. Solid black line corresponds to the spectral density expected in the inertial subrange according to Eqs. 4 and 5.

4.2 | Effect of anisotropy on the largest scales of turbulence

According to Stiperski and Calaf (2023), velocity and temperature variances are functions of both the stability parameter ζ and turbulence anisotropy y_B . Knowing that turbulence anisotropy is scale-dependent, and that the dominant anisotropy stems from the anisotropic forcing at energy-containing scales, the question arises whether y_B can explain the lack of scaling of surface-parallel velocity spectra, as well as whether the low frequency contributions among the different degrees of anisotropy show consistent behaviour.

To answer these questions, the velocity and temperature spectra are binned according to the degree of turbulence anisotropy, irrespective of ζ (Fig. 3). Spectra of surface-parallel velocities, S_u and S_v , as well as temperature S_θ , indicate a clear dependence on y_B in the range of frequencies that do not scale under the Kaimal et al. (1972) scaling. This behaviour is consistent with the results of Stiperski and Calaf (2023) for the velocity variances and shows that the degree of anisotropy is indeed the driving mechanism behind the non-scaling of surface-parallel velocity spectra. On the other hand, the surface-normal velocity spectra S_w (Fig. 3c) show only a modest dependence on y_B in terms of the energy at peak frequency: isotropic turbulence corresponds to a lower peak frequency which contains more energy than anisotropic turbulence. This dependence, however, is not uniform as an anisotropy threshold needs to be reached for y_B to show effects on the spectral peak.

Figure 3 also offers a deeper insight into the nature of turbulence eddies associated with the different degrees of anisotropy. The results show that quasi-isotropic turbulence (large y_B) is associated with smaller eddies that carry less energy in the surface-parallel, but more in the surface-normal direction than anisotropic turbulence, thus leading to an almost equal energy distribution in all the three directions. Furthermore, the peaks in the velocity spectra for

isotropic turbulence occur at similar frequencies for all three velocity components, indicating that isotropic turbulence is also quasi-isotropic in eddy size. As the anisotropy increases (y_B decreases), on the other hand, the horizontal size and the energy content of the dominant energy-containing eddies increases (the spectral peak is shifted towards lower frequencies) compared to more isotropic turbulence. In fact, the surface-normal velocity component shows strongest dependence on y_B in quasi-isotropic range, while the surface-parallel velocity spectra show largest influence in anisotropic conditions.

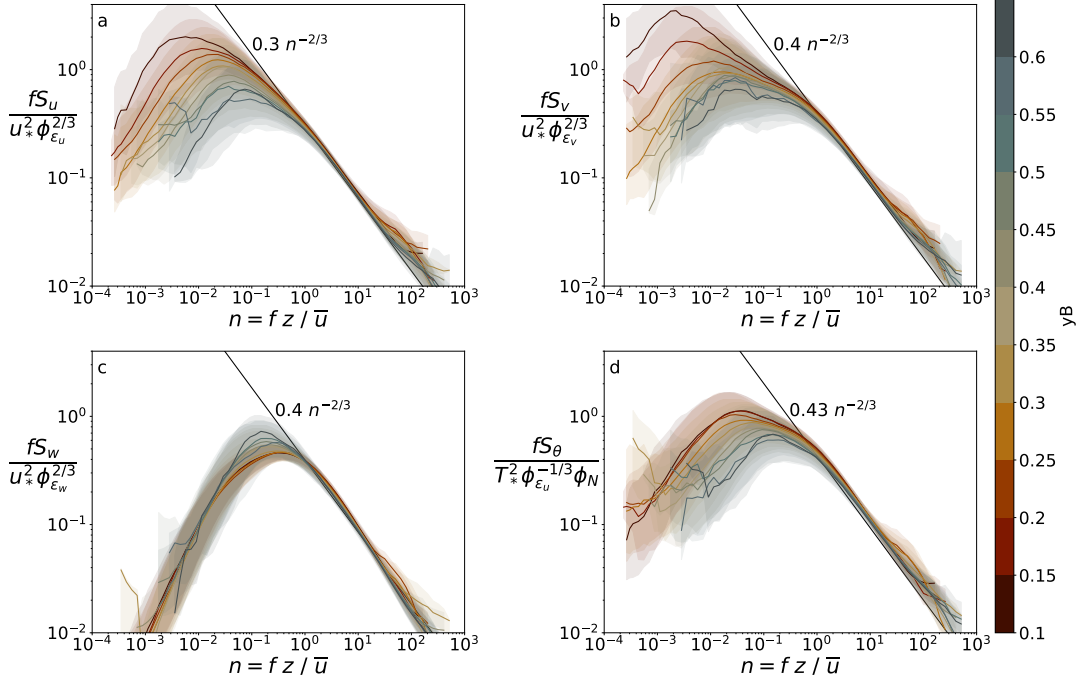


FIGURE 3 The same as Fig. 2 but binned according to the degree of anisotropy y_B (colour).

4.3 | Joint effects of turbulence anisotropy and stability

Turbulence anisotropy, while defined only based on the Reynolds stress tensor (Eqs. 17 and 18), is the result of multiple physical processes and their interactions, including stability-related processes. To separate the effect of y_B from the effect of ζ in the scaled spectra, we use the spectral peak frequency n_m of S_u as a marker. Figure 4 shows n_m as a function of y_B for the four bins of ζ defined previously (cf. Fig. 2). The behaviour of n_m differs significantly depending on whether conditions are near-neutral ($|\zeta| < 0.1$) or more convective ($|\zeta| > 0.1$). For near-neutral conditions, the spectral peak frequency increases linearly with y_B while for convective conditions the growth is exponential. For very anisotropic conditions ($y_B < 0.35$) thus the increase of n_m with y_B is weaker than in near-neutral conditions. In addition, for a given value of y_B , the spectral peak occurs at lower scaled frequencies n_m than in near-neutral stratification. This feature is lost when examining ensemble spectra binned according to ζ (Fig. 2), since each stability bin contains different anisotropy types: very anisotropic turbulence develops preferentially in near-neutral conditions,

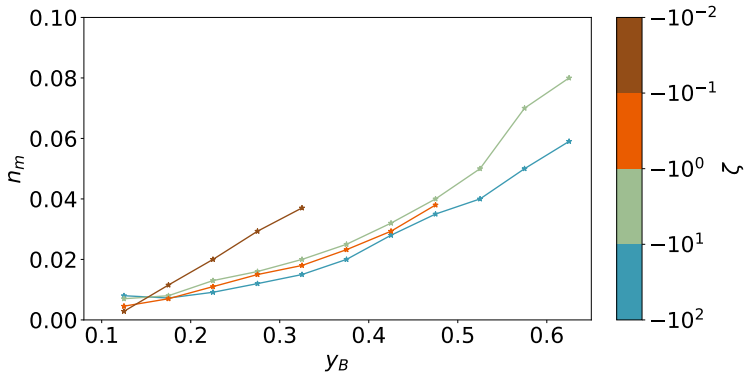


FIGURE 4 Spectral peak normalized frequency as a function of turbulence anisotropy (abscissa) and stability (colored scale). Each point is computed from the median spectra of a given bin of y_B and ζ .

while the most isotropic conditions are found only in convective conditions (Fig. 5a), as already observed in Stiperski and Calaf (2018) and Stiperski et al. (2021a)

Figure 5b-e shows the velocity and temperature spectra binned according to turbulence anisotropy for two stability classes: near-neutral ($|\zeta| < 0.1$) and highly convective ($|\zeta| > 1$). The low-frequency separation of the streamwise and spanwise velocity spectra according to y_B occurs in equal measure for near-neutral and convective conditions (Fig. 5b-c), with however several differences: (1) quasi-isotropic turbulence only occurs in convective conditions, while more anisotropic turbulence is present in all stability ranges as above-described; (2) for the most anisotropic data, the convective spectra show a well defined peak at higher frequencies than in near-neutral spectra, which instead show a plateau or a very broad peak with the maximum at lower frequencies; (3) spectral energy is higher but also more variable at low frequencies in convective conditions compared to near-neutral conditions.

The very small dependence of the surface-normal spectra on y_B (Fig. 3c) is related to the associated stability conditions (Figs. 2c and 5d). The most striking result is the small but clear increase of energy in the surface-normal direction with increasing y_B in convective conditions. The temperature spectra (Fig. 5e), on the other hand, show only a limited variability according to y_B for near-neutral stratification, but a clear separation according to anisotropy in convective conditions. The clear low frequencies binning of temperature spectra with y_B in Fig. 3d is thus the signature of the repartition of anisotropic states within the stability range considered.

Figure 5 thus clearly highlights the different characteristics of anisotropic eddies under the two stability regimes. Anisotropic eddies under near-neutral stratification are predominantly driven by shear that injects energy into the streamwise (and spanwise) velocity component. The streamwise and spanwise spectra are thus characterised by larger surface-parallel size of the most energetic eddies that occur over a wider range of scales (Fig. 5b, c), and whose size scales with height ($n = 1$) in the surface-normal direction (Fig. 5d). The anisotropic eddies that occur under convective conditions, on the other hand, have surface-parallel spectra with a better defined peak that corresponds to smaller eddies in the surface-parallel, but larger in the surface-normal direction than in near-neutral conditions. The energy content of the most energetic eddies, however, is larger than under near-neutral stratification in all three directions, especially spanwise.

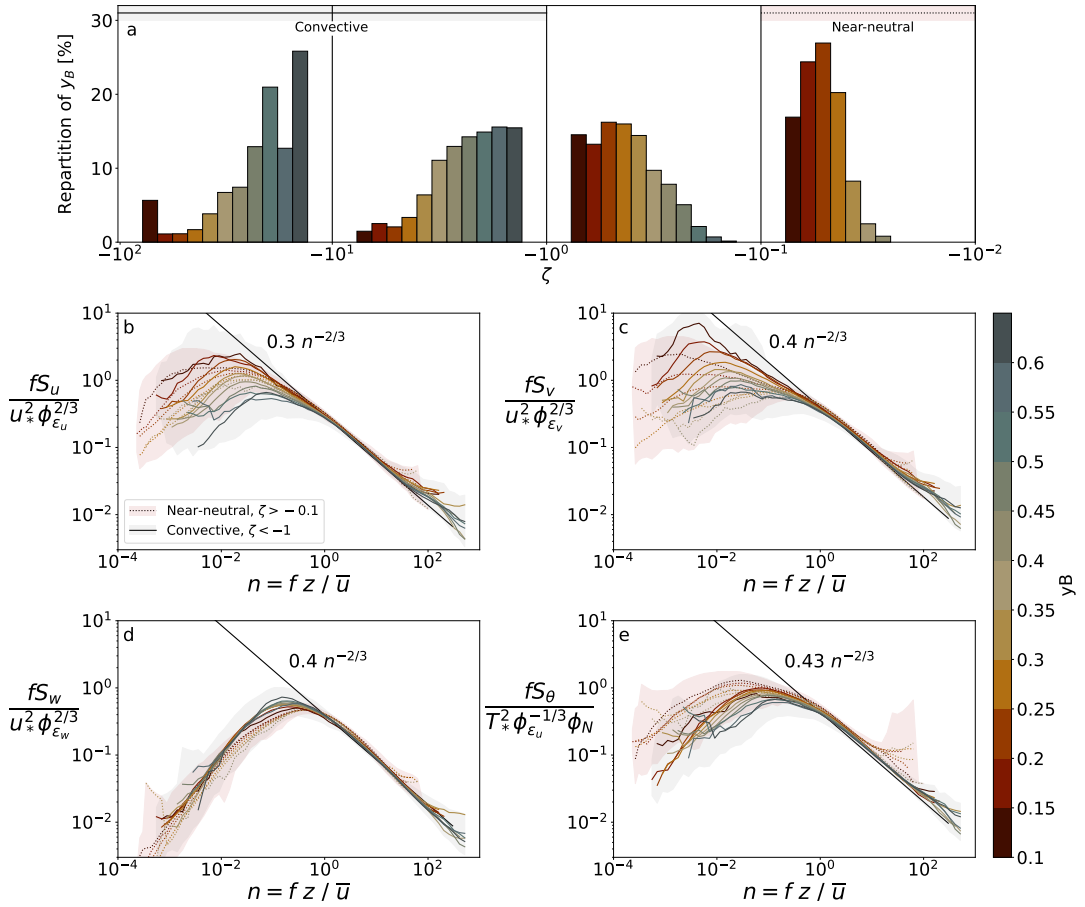


FIGURE 5 (a) Distribution of anisotropy state within each bin of ζ in the ensemble data. Spectra of (b) streamwise, (c) spanwise and (d) surface-normal velocity and of (e) temperature, binned with respect to turbulence anisotropy y_B for convective (solid lines) and near-neutral (dotted lines) conditions. The shading includes the interquartile range for the whole stability conditions considered, regardless of turbulence anisotropy bins.

TABLE 3 List of coefficients used in the spectral model, Eqs 13 and 14

Streamwise velocity spectra S_u		Spanwise velocity spectra S_v		Surface-normal velocity spectra S_w		Temperature spectra S_θ	
$\alpha = 1$	$C_u = 2.24$	$\alpha = 5/7$	$C_v = 3.09$	$\alpha = 5/4$	$C_w = 1.94$	$\alpha = 5/6$	$C_\theta = 1.8$
$\beta = 5/3$	$P = 1.5$	$\beta = 7/3$	$P = 1.07$	$\beta = 4/3$	$P = 1.875$	$\beta = 2$	$P = 1.25$
$\gamma = 1$		$\gamma = 1$		$\gamma = 1$		$\gamma = 1$	

4.4 | Analytical modeling of spectra

Following the semi-empirical model of Olesen et al. (1984) described in Sect. 2, the present Section intends to describe the spectral shape, with a function requiring only the knowledge of local parameters (namely y_B and ζ). To do so, we use Eqs. 13 and 14 and take $\gamma = 1$, as widely used in micrometeorology (cf. Kaimal et al., 1972; Olesen et al., 1984; Tieleman, 1995). As for α and β , there is no consensus on their value in the literature. In stable conditions, Olesen et al. (1984) used $\beta = 5/3$ for all three velocity components. In near-neutral conditions, Tieleman (1995) differentiates between ideal terrain (flat, smooth and uniform), where $\beta = 1$ is the best fit, and complex terrain (heterogeneous surface roughness, topography conditions), where $\beta = 5/3$ is more suitable. According to Kaimal (1978), a value of $5/3$ is also the best fit for the surface-normal velocity spectra in unstable conditions. In the present paper, we adapted β , without any a priori assumptions, to the value that fits best to the spectra. We observe that $\beta = 5/3$ is a good fitting parameter only for S_u , while S_v and S_w require respectively $7/3$ and $4/3$, and S_θ is best described by $\beta = 2$. The remaining exponent α is derived from Eq. 9, knowing β and γ . These coefficients, and the resulting parameters, used to derive the solution are summarized in Table 3.

Figure 6 shows the velocity and temperature spectra along with the model predictions. The model, given by Eq. 13 when ϕ_{u_i} and ϕ_ε are determined directly from the data (Eq. 6 and 12), is able to capture well the behaviour of velocity spectra, including the low frequency spectral variation and the shift of the spectral peak with turbulence anisotropy (Fig. 6a, 6d and 6g). For the streamwise velocity spectra, the main divergence is that the model underestimates slightly the energy peak. This is more pronounced for very anisotropic turbulence and tends to disappear as y_B increases. We also note an inability of the model - constrained by its mathematical shape - to reproduce the concave region of S_v at high anisotropy. Except for these details, we thus consider that the mathematical shape of the model is good enough to be used thereafter for all velocity components.

Because of the inability of MOST to describe properly horizontal velocity variances under unstable stratification, it was not possible to compute correct spectral behaviour for horizontal velocity spectra using the $\phi(\zeta)$ functions, when the model of Olesen et al. (1984) was published. Figures 6b and 6e, indeed show a huge discrepancy between the predictions of Eq. 13 when using the classic MOST ϕ functions (left column in Table 1) and the data both in terms of low frequency spectral energy and position of the spectral peak. The discrepancy is particularly obvious for isotropic turbulence in streamwise and all anisotropy types in spanwise velocity spectra. Sect. 4.2 showed that S_u and S_v are strongly dependant on y_B . Figures 6c and 6f confirm that when using ϕ_{u_i} , $\phi_\varepsilon = f(y_B, \zeta)$ (right column in Table 1) as parameters of the model, we are now able to better predict the shape of the spectra based only on stability ζ and turbulence anisotropy y_B as input parameters. Note that due to a lack of scaling relation for ϕ_{ε_v} in Stiperski and Calaf (2023) and under the commonly applied assumption of horizontal isotropy, we used ϕ_{ε_u} also in the spanwise velocity spectra. For the surface-normal spectra, the discrepancy between the data and the model based on MOST (Fig. 6h) is small, because $\phi_w = f(\zeta)$ was already a good approximation in the MOST framework (left column in Table 1). When

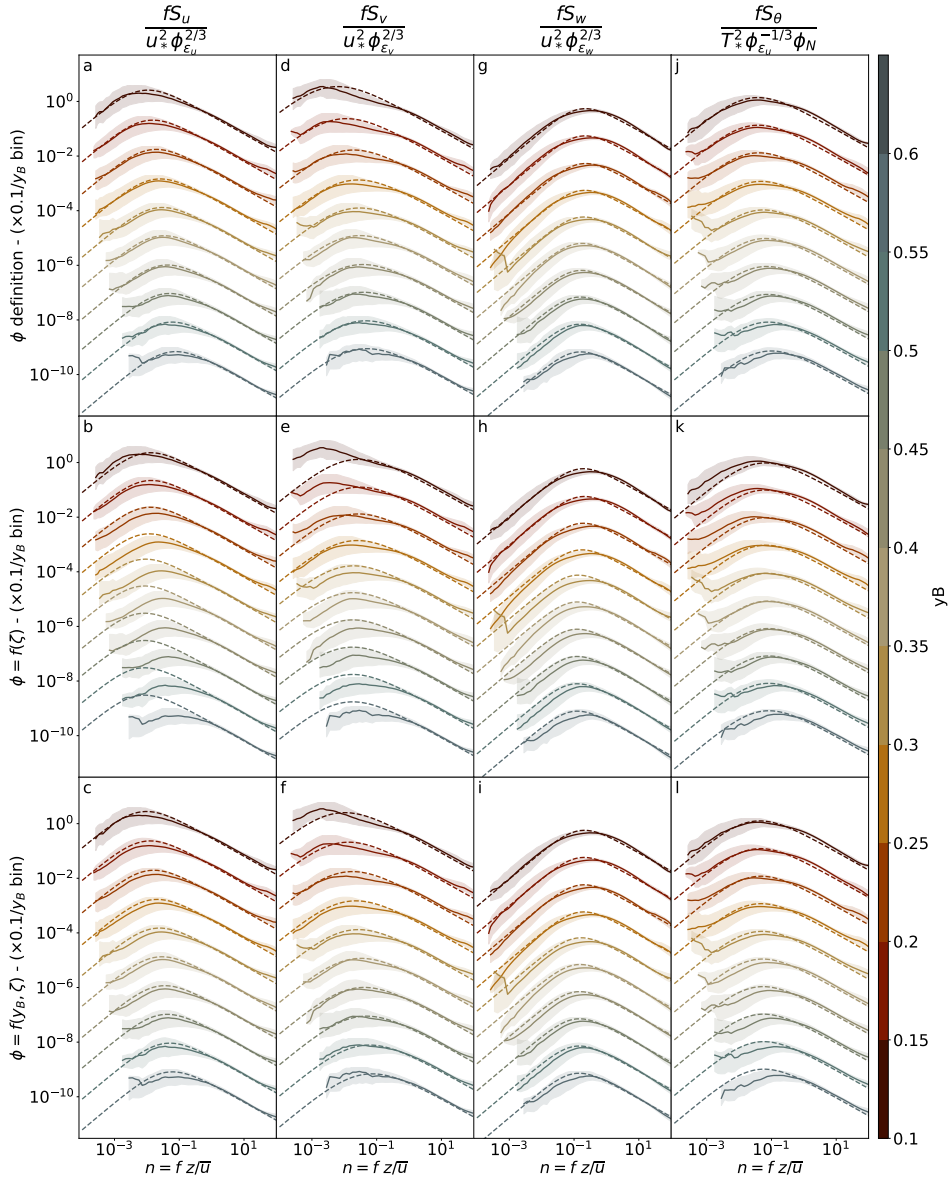


FIGURE 6 Scaled (a-c) streamwise, (d-f) spanwise, (g-i) surface-normal velocity spectra and (j-l) temperature spectra. In each subplot, the solid lines represent the median of a range of turbulence anisotropy from the ensemble data of simple terrain dataset. The dashed lines are the solution of Olesen’s model, computed for each individual spectrum before taking their median. The shading is the interquartile range for each anisotropy bin (scale on the right for the corresponding values of y_B). In the first row, the solution is computed using the definition of ϕ (Eqs. 6, 7, 12 and 16), the second row when using the ϕ functions according to MOST, and third row when using ϕ functions according to Stiperski and Calaf (2023) (Table 1). To facilitate the reading, spectra in each subplot are shifted down compared to each other by one decade, where the upper-most spectrum is in the correct position.

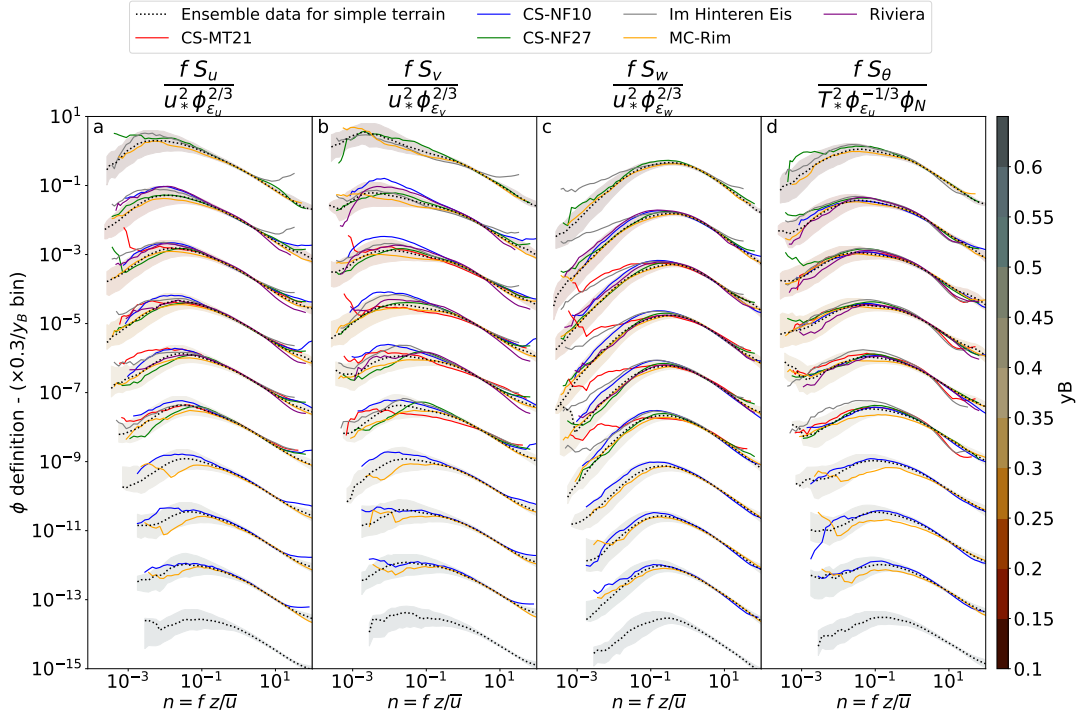


FIGURE 7 Scaled (a) streamwise, (b) spanwise, (c) surface-normal velocity spectra and (d) temperature spectra. In each subplot, the black dotted lines represent the median of a range of turbulence anisotropy from the ensemble data of simple terrain dataset. The shading is the interquartile range for each bin of anisotropy bin (scale on the right for the corresponding values of y_B). The colored solid lines are the median of the spectra per bin of y_B for each of the 6 datasets included in the complex mountainous category. To facilitate the reading, spectra in each subplot are shifted down compared to each other by 0.3, where the upper-most spectrum is in the correct position.

using the ϕ_w , $\phi_\varepsilon = f(y_B, \zeta)$ functions (right column in Table 1), as parameters of the model, the spectra are, however, now even better represented (Fig. 6i).

The model applied to temperature spectra (Eq. 14) using Eqs. 6, 7 and 16, is shown in Fig. 6j. The solution based on MOST ϕ functions is relatively good, with mostly a slight underestimation of low frequency spectral energy for the most anisotropic bins (Fig. 6k). This is not a surprise provided that both ϕ_θ , ϕ_ε and ϕ_N are already well approximated by MOST. This confirms that the spread observed in Fig. 3d is mostly linked to ζ . Furthermore, Stiperski and Calaf (2023) showed that ϕ_θ does not depend strongly on y_B away from near-neutral stratification, while ϕ_ε has a limited dependence on y_B in the stability range considered. If we now use ϕ_θ and $\phi_\varepsilon = f(y_B, \zeta)$ and keep $\phi_N = f(\zeta)$ (cf. Table 1), the model improves for low y_B , while MOST scaling relations performs best for $y_B > 0.45$. The reason for using MOST function for ϕ_N stems from no scaling relation for ϕ_N in Stiperski and Calaf (2023), as well as no clear dependence on y_B is observed in the data (not shown).

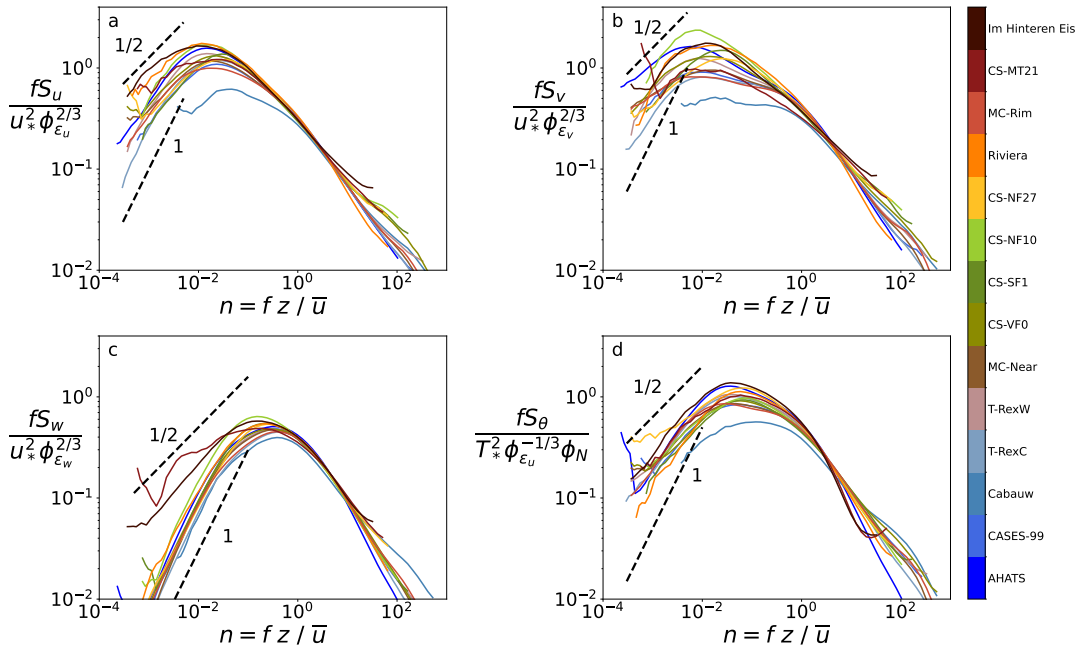


FIGURE 8 Median scaled spectra of (a) streamwise, (b) spanwise and (c) surface-normal velocity and (d) temperature for each individual dataset. Datasets are classified on the scale from the simplest (blue) to the most complex (red). The black dashed lines indicate spectral slopes of $1/2$ and 1 .

4.5 | Spectral scaling in mountainous terrain

For near-neutral stability conditions, Tieleman (1995) reported that the large scale behaviour of S_u and S_v is highly related to the upwind topography, causing differences in the spectra from one site to another, both in shape and in spectral energy. Over mountainous terrain, this behaviour is expected to be even more pronounced since the upwind topography is highly direction dependent. The scaling results (Fig. 7) show that terrain indeed influences the spectral distribution since the datasets show a large divergence amongst themselves, but also that the effect of terrain is anisotropy dependent. For the majority of the anisotropy range ($y_B > 0.35$), the median spectra of six mountainous datasets mostly fall within the spread of the simple terrain datasets, despite the strong terrain complexity and the expected effect of heterogeneity on the low frequency motions. For very anisotropic turbulence ($y_B < 0.3$), however, spectra of all three velocity components over complex terrain are found to always be above the simple terrain median, the spectral peak is shifted towards larger scales and the low frequency energy increases for S_u , S_v and S_θ as y_B decreases. The surface-normal spectra S_w , on the other hand, show an increase of the spectral energy around the frequency of the energy peak when approaching isotropy, as well as a secondary peak for some datasets (cf. CS-MT21). It thus appears that terrain complexity mostly impacts the surface-parallel components more for anisotropic turbulence, and surface-normal component more for isotropic turbulence.

According to Tieleman (1995), the scaled complex terrain spectra are characterized by a low frequency energy higher than simple terrain spectra and a slope γ lower than 1 at these frequencies (although what they consider as complex terrain is flat terrain with a ridge located 400 m from the measurement site, similar to T-REX which we characterize as simple terrain in our study, Perry et al., 1978; Panofsky et al., 1982). Among the 14 datasets used in

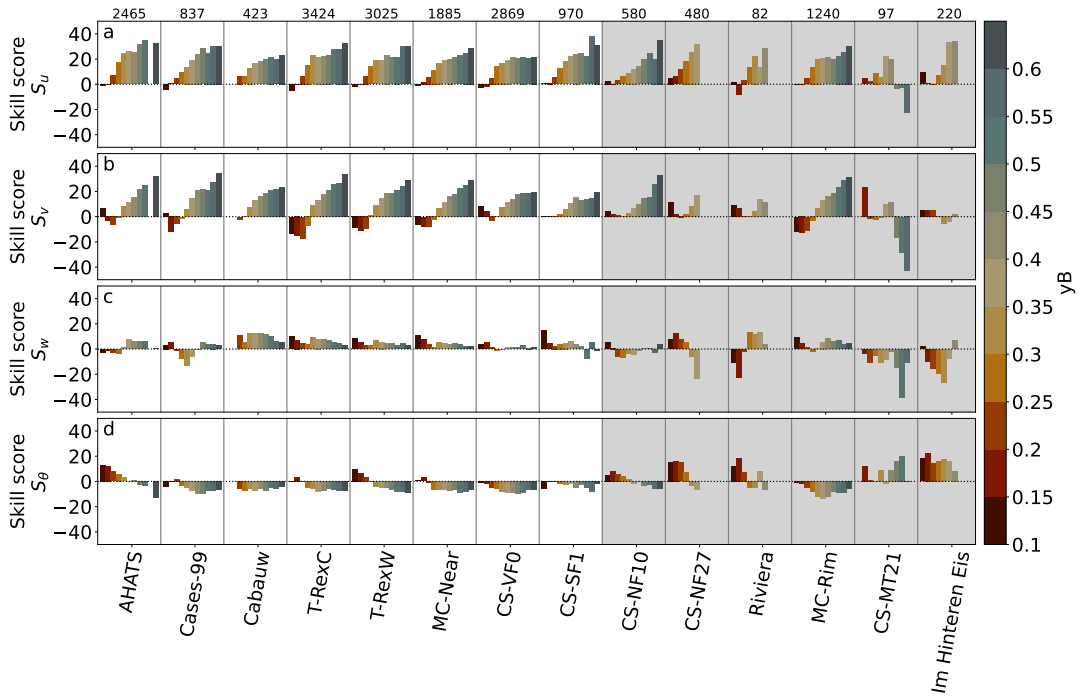


FIGURE 9 Skill score of the improvement of the spectral model based on $\phi = f(y_B, \zeta)$ over the model using the original MOST ϕ functions, for (a) the streamwise velocity spectra, (b) the spanwise velocity spectra, (c) the surface-normal velocity spectra and (d) the temperature spectra for each of the dataset used in the present study. The bins color corresponds to turbulence anisotropy state. White and gray backgrounds are used for simple and complex terrain respectively. The number of 30-min segments of each dataset is indicated at the top of each column.

the present study, we also observe a reduction of the low frequency slope of S_u and S_v , when spectra are plotted as the median over the whole dataset (Fig. 8). This slope decreases from nearly 1 for some of the simple terrain down to about 0.5 for the most complex terrain. Median temperature spectra S_θ show a low frequency slope lower than 1 for all of the datasets acquired over simple and complex terrain. However, when binned according to y_B , low frequency slopes of both velocity and temperature spectra are closer to 1, hence the use of $\gamma = 1$ in the analytical model. Thus the slope decrease mentioned by Tieleman (1995) and observed in Fig. 8 could be the result of the averaging of spectra for data acquired over different conditions (stability, turbulence anisotropy, wind direction etc.). Interestingly, low frequency slopes of S_w , whether binned according to turbulence anisotropy conditions or not, are about 1, except for the two most complex terrain datasets (Im Hinteren Eis and CS-MT21), for which γ is lower. This feature is observed for all anisotropy conditions (Fig. 7).

5 | DISCUSSION

5.1 | Performance of the new spectral scaling

Figure 9 quantifies the improvement of the model brought by using the scaling relations of Stiperski and Calaf (2023) over using MOST (Table 1) for each bin of y_B in each of the datasets, through the skill score S_s . The skill score is defined based on the mean absolute deviation (MAD) of the spectra, as:

$$S_s = 1 - \frac{MAD_{f(y_B, \zeta)}}{MAD_{f(\zeta)}}, \quad (21)$$

with:

$$MAD = \frac{1}{T} \sum_{t=1}^T \left(\frac{1}{N} \sum_{i=1}^N |\log(S_{\text{model}}^t(n_i)) - \log(S_{\text{data}}^t(n_i))| \right), \quad (22)$$

where $S_{\text{model}}^t(n_i)$ and $S_{\text{data}}^t(n_i)$ are the spectra from the analytical model – either $f(y_B, \zeta)$ or $f(\zeta)$ – and from the data respectively, at the normalized frequency n_i (N is the number of frequency points within each spectra) and for the time segment t (T is the number of time segments within each dataset). The skill score is computed for each individual spectrum and the result is the average value per bin of y_B .

The skill score indicates a net improvement of the ability of the model to reproduce the surface-parallel velocity spectra, by up to about 30%, when using $f(y_B, \zeta)$ compared to $f(\zeta)$, for both the simple and the complex terrain (Fig. 9). The negative values for very anisotropic conditions and the low values for intermediate anisotropic conditions in Fig. 9 are the result of the shape constraint of the model, which does not allow to correctly capture the energy peak for the most anisotropic bins (Sect. 4.4). Qualitatively, looking at the individual datasets, the model is indeed still better in its new version including y_B : the model using $f(\zeta)$ overestimates the energy peak and underestimate the lowest frequencies, while the model using $f(y_B, \zeta)$ only overestimates the energy peak but can reproduce well the low frequencies. The surface-normal velocity spectra, that were found not to be strongly influenced by anisotropy, are also improved, but to a lesser degree (up to about 10%), for most of the simple terrain datasets. There is no coherent pattern, however, over complex terrain.

Section 4.4 demonstrated that the prediction of temperature spectra for the most anisotropic conditions is improved by the use of y_B in the model whereas it is worsened for the less anisotropic spectra for simple terrain. Looking at each dataset separately, this behaviour is still globally valid for simple terrain but the behaviour of the most anisotropic bins is not always improved. This is also observed for the datasets acquired over sloping terrain (CS-NF10, CS-NF27, Riviera) with a clear improvement of the prediction of very anisotropic temperature spectra by up to about 15%. Mountain top stations (CS-MT21, Im Hinteren Eis) show a relevant improvement for all anisotropic conditions, as well.

Interestingly, spectra computed with data from MC-Rim station (Table 2), located at the rim of a meteor crater, are not strongly affected by the complexity of the surrounding terrain neither for velocity components nor for temperature. This might be due to the fetch since only 25% of the 30-min segments retained after quality control (Sect. 3.2) originates from the direction of the crater while the rest originate from a more uniform terrain, like MC-NEAR station.

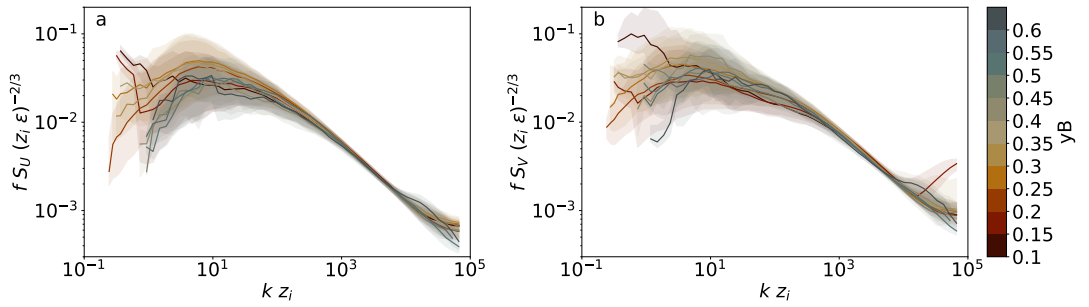


FIGURE 10 Scaled spectra of (a) streamwise and (b) spanwise velocity component for the T-RexW dataset, scaled according to McNaughton et al. (2007) with the ML height z_i .

5.2 | Discussion on the mixing layer scaling of velocity spectra

The mixed layer scaling approach of Panofsky et al. (1977) for horizontal velocity variances and its expansion to velocity and temperature spectra (McNaughton et al., 2007) was developed in response to the failure of MOST. ML scaling states that the dynamics of horizontal velocity fluctuations is governed by the ML height z_i as a relevant length scale. Stiperski and Calaf (2023) showed that mixed layer scaling does collapse the surface-parallel velocity variances better than MOST, however, with a lingering dependence on anisotropy. We therefore explore the ML spectral scaling approach of McNaughton et al. (2007) in light of anisotropy. For this we use the data from the West tower during T-REX campaign (cf. Table 2), as lidar observations at this site allowed retrieving the information on z_i .

Figure 10 shows scaled streamwise and spanwise velocity spectra for which z_i , instead of the measurement height z , is taken to be the representative length scale. The clear separation of the low frequency spectral energy and the shift of the spectral peak position for surface-parallel velocity spectra with y_B observed in Fig. 3 nearly disappear (Fig. 10). Only a slight shift of the spectral peak position for S_u is observed, by about one decade whereas it was of about three decades in Fig. 3. These results confirm the importance of ML height in the surface-parallel velocity dynamics.

As expected since ϕ_w and S_w follow MOST, the mixed layer scaling applied to S_w shows the opposite behaviour (Fig. 11a), namely an evident dependence on y_B at low frequency, both in terms of spectral energy and peak position: low frequency spectral energy increases and spectral peaks are shifted towards larger scales as anisotropy decreases. This shift of the low frequency spectral energy in S_w is linked to the relative height of the measurements within the mixed layer, and can be corrected by the factor $(z/z_i)^{-2}$ (Fig. 11b), derived from Fig. 5 of McNaughton et al. (2007). However, this causes the spectra not to scale in the inertial subrange.

The comparison between Figs. 3 and 10 indicates that ML height does impose an important scale on surface-parallel velocity spectra, but does not integrate all of the processes affecting them. In fact, S_u and S_v scaled according to ML approach, still exhibit significant scatter and a weak dependence on y_B , charting the limitations of the ML approach.

6 | CONCLUSION

Turbulence anisotropy has been shown to improve flux-variance and flux-gradient scaling under Monin-Obukhov similarity theory (MOST) and allow it to be extended to conditions where the assumptions of MOST are clearly violated

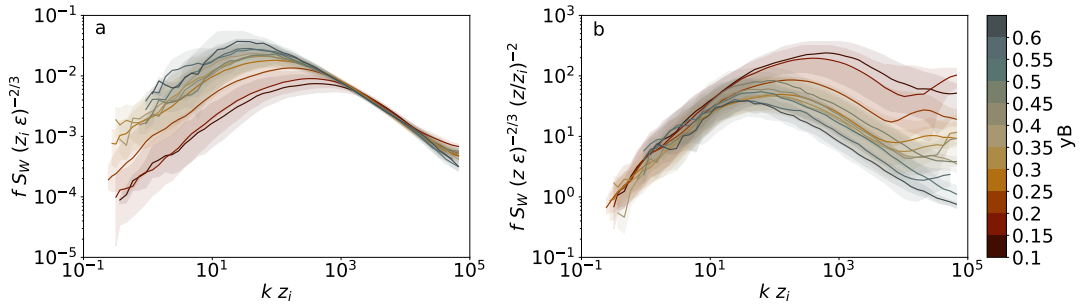


FIGURE 11 Surface-normal velocity spectra from the T-RexW dataset, scaled according to McNaughton et al. (2007) (a) with the ML height z_i , and (b) using a combination of the the ML height z_i and the measurement height z as the representative length scales.

(Stiperski and Calaf, 2023; Mosso et al., 2023). Here we expended these findings to spectral scaling in the unstable surface layer ($-100 < \zeta < -0.01$) known not to obey MOST. We examined the combined role of turbulence anisotropy y_B and stability ζ in explaining the dynamics of the largest turbulent scales, through the analysis of velocity and temperature spectra scaled using inertial subrange properties (Kolmogorov, 1941a,b) and MOST. Our analysis, based on an ensemble of 14 datasets covering a wide range of stability and surface conditions, demonstrated that turbulence anisotropy y_B is able to explain the low frequency spread and the position of the spectral peak in both the scaled streamwise and spanwise velocity spectra, with a secondary effect of stability ζ . On the other hand, stability was shown to be the primary factor able to relate the spread of the largest scales in temperature spectra and the peak position and intensity for both temperature and surface-normal velocity spectra, while y_B was shown to have a secondary effect, most pronounced in convective conditions. The combination of ζ and y_B in a semi-empirical model was therefore shown to be a powerful tool to describe the behaviour of the three velocity components and temperature spectra.

The spectral scaling results shed light on the nature of turbulent eddies under different states of anisotropy. Anisotropy was shown to govern the spectral peak position, so that anisotropic turbulence is characterized by eddies that peak at lower frequencies in the surface-parallel velocities and temperature spectra, and to carry larger fraction of variance than isotropic turbulence. On the other hand, isotropic turbulence, preferentially occurring in convective conditions, was shown to be comprised of eddies that are smaller in size both in spectra of streamwise and spanwise velocity and temperature, and to carry a smaller fraction of energy than anisotropic turbulence. In addition, isotropic turbulence was shown to be quasi-isotropic not only in energy but also in size of the energy containing eddies. Finally, the results highlighted that the spectral characteristics of anisotropic eddies depend on stratification, so that anisotropic turbulence under near-neutral and very unstable conditions differ.

The complementary analysis of six datasets acquired over highly complex mountainous terrain is a first of its kind to systematically explore the impact of highly complex terrain on turbulence spectra. We note a net improvement of the ability to describe the surface-parallel velocity spectra S_u and S_v in complex terrain when incorporating y_B into the analysis, compared to when using only ζ . Complexity of turbulence in velocity and temperature spectra are quite well predicted through the semi-empirical model, including y_B and ζ as parameters, for data acquired on steep slopes. For mountain top locations, however, the spectral model has only limited ability. The cause of this might stem from the use of double rotation, which might incorrectly assign the velocity variances compared to the gravity vector especially under conditions of flow separation. In addition, other factors not taken into account might play a role, such

as for example streamline curvature.

In the end, we explored the contribution of the mixed layer scaling to the understanding of the largest scales of turbulence for velocity spectra, and found that, as previously observed, including the mixed layer height instead of measurement height into scaling reduced the low frequency spread of S_u and S_v . This approach, however, still exhibited large scatter and a weak dependence on anisotropy, and therefore did not outperform the Kaimal scaling with included anisotropy.

The present study highlights the advantage of examining a wide range of stability and surface conditions in gaining insights into the complex surface-layer dynamics. Thus, the clear dependence of temperature spectra on stability ζ , not observed by Kaimal et al. (1972), is here shown to emerge out of the extensive stability range probed. The results further highlight that turbulence anisotropy, quantified through the invariant y_B , is not only a powerful tool in expanding flux-variance, flux-gradient and spectral scaling to non-canonical conditions, but through the modified spectral scaling offers a deeper understanding of the nature and physical processes driving surface-layer turbulence, both over canonical and complex surfaces.

Acknowledgements

The providers of various data sets are acknowledged: the managers of the database of the Cabauw Experimental Site for Atmospheric Research (CESAR), UCAR/NCAR - Earth Observing Laboratory (EOL) for the access to the AHATS, CASES-99, METCRAX II and T-REX data sets, the University of Basel and ETH for the Riviera dataset, and all the collaborators of Department of Atmospheric and Cryospheric Sciences (ACINN), who worked for many years to make the reliable and continuous database of the i-Box study area, and Im Hinteren Eis station available.

Conflict of interest

The authors declare no conflict of interest.

references

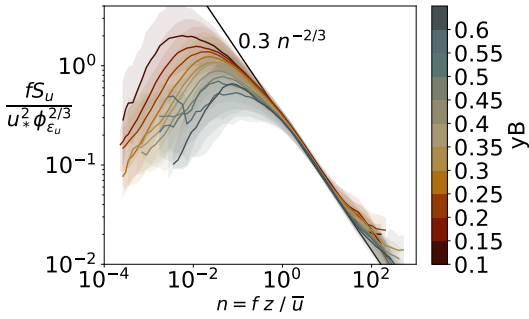
- Aubinet, M., Vesala, T. and Papale, D. (2012) *Eddy covariance: a practical guide to measurement and data analysis*. Springer Science & Business Media.
- Babić, N., Večenaj, Ž. and De Wekker, S. F. (2017) Spectral gap characteristics in a daytime valley boundary layer. *Quarterly Journal of the Royal Meteorological Society*, **143**, 2509–2523.
- Babić, K. and Rotach, M. W. (2018) Turbulence kinetic energy budget in the stable boundary layer over a heterogeneous surface. *Quarterly Journal of the Royal Meteorological Society*, **144**, 1045–1062.
- Banerjee, S., Krahl, R., Durst, F. and Zenger, C. (2007) Presentation of anisotropy properties of turbulence, invariants versus eigenvalue approaches. *Journal of Turbulence*, N32.
- Banerjee, T., Katul, G., Salesky, S. and Chamecki, M. (2015) Revisiting the formulations for the longitudinal velocity variance in the unstable atmospheric surface layer. *Quarterly Journal of the Royal Meteorological Society*, **141**, 1699–1711.
- Caughy, S. (1977) Boundary-layer turbulence spectra in stable conditions. *Boundary-Layer Meteorology*, **11**, 3–14.
- Chamecki, M. and Dias, N. L. (2004) The local isotropy hypothesis and the turbulent kinetic energy dissipation rate in the atmospheric surface layer. *Quarterly Journal of the Royal Meteorological Society*, **130**, 2733–2752.

- Dairay, T., Lamballais, E., Laizet, S. and Vassilicos, J. C. (2017) Numerical dissipation vs. subgrid-scale modelling for large eddy simulation. *Journal of Computational Physics*, **337**, 252–274.
- De Franceschi, M., Zardi, D., Tagliuzucca, M. and Tampieri, F. (2009) Analysis of second-order moments in surface layer turbulence in an alpine valley. *Quarterly Journal of the Royal Meteorological Society: A journal of the atmospheric sciences, applied meteorology and physical oceanography*, **135**, 1750–1765.
- Dupont, S. and Patton, E. G. (2022) On the influence of large-scale atmospheric motions on near-surface turbulence: comparison between flows over low-roughness and tall vegetation canopies. *Boundary-Layer Meteorology*, **184**, 195–230.
- Foken, T. and Wichura, B. (1996) Tools for quality assessment of surface-based flux measurements. *Agricultural and Forest Meteorology*, **78**, 83–105.
- Gibbs, J. A. and Fedorovich, E. (2014) Comparison of convective boundary layer velocity spectra retrieved from large-eddy-simulation and weather research and forecasting model data. *Journal of Applied Meteorology and Climatology*, **53**, 377–394.
- Gioia, G., Guttenberg, N., Goldenfeld, N. and Chakraborty, P. (2010) Spectral theory of the turbulent mean-velocity profile. *Physical Review Letters*, **105**, 184501.
- Grubišić, V., Doyle, J. D., Kuettner, J., Mobbs, S., Smith, R. B., Whiteman, C. D., Dirks, R., Czyzyk, S., Cohn, S. A., Vosper, S. et al. (2008) The terrain-induced rotor experiment: A field campaign overview including observational highlights. *Bulletin of the American Meteorological Society*, **89**, 1513–1534.
- Haugen, D., Kaimal, J. and Bradley, E. (1971) An experimental study of reynolds stress and heat flux in the atmospheric surface layer. *Quarterly Journal of the Royal Meteorological Society*, **97**, 168–180.
- Horst, T., Kleissl, J., Lenschow, D. H., Meneveau, C., Moeng, C.-H., Parlange, M., Sullivan, P. and Weil, J. (2004) HATS: Field observations to obtain spatially filtered turbulence fields from crosswind arrays of sonic anemometers in the atmospheric surface layer. *Journal of the atmospheric sciences*, **61**, 1566–1581.
- Kader, B. and Yaglom, A. (1990) Mean fields and fluctuation moments in unstably stratified turbulent boundary layers. *Journal of Fluid Mechanics*, **212**, 637–662.
- Kaimal, J. (1973) Turbulence spectra, length scales and structure parameters in the stable surface layer. *Boundary-Layer Meteorology*, **4**, 289–309.
- (1978) Horizontal velocity spectra in an unstable surface layer. *Journal of Atmospheric Sciences*, **35**, 18–24.
- Kaimal, J. C. and Finnigan, J. J. (1994) *Atmospheric boundary layer flows: their structure and measurement*. Oxford university press.
- Kaimal, J. C., Wyngaard, J., Izumi, Y. and Coté, O. (1972) Spectral characteristics of surface-layer turbulence. *Quarterly Journal of the Royal Meteorological Society*, **98**, 563–589.
- Katul, G. G., Konings, A. G. and Porporato, A. (2011) Mean velocity profile in a sheared and thermally stratified atmospheric boundary layer. *Physical Review Letters*, **107**, 268502.
- Katul, G. G., Li, D., Chamecki, M. and Bou-Zeid, E. (2013) Mean scalar concentration profile in a sheared and thermally stratified atmospheric surface layer. *Physical Review E*, **87**, 023004.
- Katul, G. G., Porporato, A., Shah, S. and Bou-Zeid, E. (2014) Two phenomenological constants explain similarity laws in stably stratified turbulence. *Physical Review E*, **89**, 023007.
- Kiely, G., Albertson, J. D., Parlange, M. B. and Eichinger, W. E. (1996) Convective scaling of the average dissipation rate of temperature variance in the atmospheric surface layer. *Boundary-Layer Meteorology*, **77**, 267–284.
- Kolmogorov, A. (1941a) Dissipation of energy in locally isotropic turbulence. *Doklady Akademii Nauk SSSR*, **32**, 19–21.

- (1941b) The local structure of turbulence in incompressible viscous fluid for very large Reynolds numbers. *Dokl. Akad. Nauk SSSR*, **30**, 299–303.
- Lan, C., Liu, H., Katul, G. G., Li, D. and Finn, D. (2022) Turbulence structures in the very stable boundary layer under the influence of wind profile distortion. *Journal of Geophysical Research: Atmospheres*, **127**, e2022JD036565.
- Laubach, J. and McNaughton, K. G. (2009) Scaling properties of temperature spectra and heat-flux cospectra in the surface friction layer beneath an unstable outer layer. *Boundary-Layer Meteorology*, **133**, 219–252.
- Lehner, M., Whiteman, C. D., Hoch, S. W., Crosman, E. T., Jeglum, M. E., Cherukuru, N. W., Calhoun, R., Adler, B., Kalthoff, N., Rotunno, R. et al. (2016) The METCRAX II field experiment: A study of downslope windstorm-type flows in Arizona's Meteor Crater. *Bulletin of the American Meteorological Society*, **97**, 217–235.
- Li, D. (2021) The O'KEYPS equation and 60 years beyond. *Boundary-Layer Meteorology*, **179**, 19–42.
- Lumley, J. L. (1978) Computational modeling of turbulent flows. *Advances in Applied Mechanics*, **18**, 123–176.
- McNaughton, K., Clement, R. and Moncrieff, J. (2007) Scaling properties of velocity and temperature spectra above the surface friction layer in a convective atmospheric boundary layer. *Nonlinear Processes in Geophysics*, **14**, 257–271.
- Monin, A. S. and Obukhov, A. M. (1954) Osnovnye zakonomernosti turbulentnogo peremeshivaniya v prizemnom sloe atmosfery (basic laws of turbulent mixing in the atmosphere near the ground). *Trudy Geofizicheskogo Instituta, Akademiya Nauk SSSR*, **24**, 163–187.
- Mosso, S., Calaf, M. and Stiperski, I. (2023) Flux gradient relations and their dependence on turbulence anisotropy. *Quarterly Journal of the Royal Meteorological Society*, <https://doi.org/10.48550/arXiv.2310.07503>.
- Nadeau, D. F., Pardyjak, E. R., Higgins, C. W. and Parlange, M. B. (2013) Similarity scaling over a steep alpine slope. *Boundary-Layer Meteorology*, **147**, 401–419.
- Nieuwstadt, F. (1984) Some aspects of the turbulent stable boundary layer. *Boundary Layer Structure: Modeling and Application to Air Pollution and Wind Energy*, 31–55.
- Olesen, H., Larsen, S. E. and Højstrup, J. (1984) Modelling velocity spectra in the lower part of the planetary boundary layer. *Boundary-Layer Meteorology*, **29**, 285–312.
- Panofsky, H., Larko, D., Lipschut, R., Stone, G., Bradley, E., Bowen, A. J. and Højstrup, J. (1982) Spectra of velocity components over complex terrain. *Quarterly Journal of the Royal Meteorological Society*, **108**, 215–230.
- Panofsky, H. A., Tennekes, H., Lenschow, D. H. and Wyngaard, J. (1977) The characteristics of turbulent velocity components in the surface layer under convective conditions. *Boundary-Layer Meteorology*, **11**, 355–361.
- Perry, S. G., Norman, J. M., Panofsky, H. A. and Martsof, J. D. (1978) Horizontal coherence decay near large mesoscale variations in topography. *Journal of Atmospheric Sciences*, **35**, 1884–1889.
- Pope, S. B. (2000) *Turbulent flows*. Cambridge university press.
- Poulos, G. S., Blumen, W., Fritts, D. C., Lundquist, J. K., Sun, J., Burns, S. P., Nappo, C., Banta, R., Newsom, R., Cuxart, J. et al. (2002) Cases-99: A comprehensive investigation of the stable nocturnal boundary layer. *Bulletin of the American Meteorological Society*, **83**, 555–582.
- Rotach, M. (1995) Profiles of turbulence statistics in and above an urban street canyon. *Atmospheric Environment*, **29**, 1473–1486.
- Rotach, M. W., Calanca, P., Graziani, G., Gurtz, J., Steyn, D. G., Vogt, R., Andretta, M., Christen, A., Cieslik, S., Connolly, R. et al. (2004) Turbulence structure and exchange processes in an alpine valley: the Riviera project. *Bulletin of the American Meteorological Society*, **85**, 1367–1386.

- Rotach, M. W., Stiperski, I., Fuhrer, O., Goger, B., Gohm, A., Obleitner, F., Rau, G., Sfyri, E. and Vergeiner, J. (2017) Investigating exchange processes over complex topography: the Innsbruck box (i-Box). *Bulletin of the American Meteorological Society*, **98**, 787–805.
- Salesky, S. and Anderson, W. (2018) Buoyancy effects on large-scale motions in convective atmospheric boundary layers: implications for modulation of near-wall processes. *Journal of Fluid Mechanics*, **856**, 135–168.
- Sfyri, E., Rotach, M. W., Stiperski, I., Bosveld, F. C., Lehner, M. and Obleitner, F. (2018) Scalar-flux similarity in the layer near the surface over mountainous terrain. *Boundary-Layer Meteorology*, **169**, 11–46.
- Stiperski, I. and Calaf, M. (2018) Dependence of near-surface similarity scaling on the anisotropy of atmospheric turbulence. *Quarterly Journal of the Royal Meteorological Society*, **144**, 641–657.
- (2023) Generalizing Monin-Obukhov similarity theory (1954) for complex atmospheric turbulence. *Physical Review Letters*, **130**, 124001.1–124001.7.
- Stiperski, I., Calaf, M. and Rotach, M. W. (2019) Scaling, anisotropy, and complexity in near-surface atmospheric turbulence. *Journal of Geophysical Research: Atmosphere*, **124**, 1428–1448.
- Stiperski, I., Chamecki, M. and Calaf, M. (2021a) Anisotropy of unstably stratified near-surface turbulence. *Boundary-Layer Meteorology*, **180**, 363–384.
- Stiperski, I., Holtslag, A. A. M., Lehner, M., Hoch, S. W. and Whiteman, C. D. (2020) On the turbulence structure of deep katabatic flows on a gentle mesoscale slope. *Quarterly Journal of the Royal Meteorological Society*, **146**, 1206–1231.
- Stiperski, I., Katul, G. G. and Calaf, M. (2021b) Universal return to isotropy of inhomogeneous atmospheric boundary layer turbulence. *Physical Review Letters*, **126**, 194501.
- Stull, R. B. (1988) *An introduction to boundary layer meteorology*, vol. 13. Springer Science & Business Media.
- Sukoriansky, S., Galperin, B. and Perov, V. (2005) Application of a new spectral theory of stably stratified turbulence to the atmospheric boundary layer over sea ice. *Boundary-Layer Meteorology*, **117**, 231–257.
- Sun, J., Takle, E. S. and Acevedo, O. C. (2020) Understanding physical processes represented by the monin-obukhov bulk formula for momentum transfer. *Boundary-Layer Meteorology*, **177**, 69–95.
- Taylor, G. I. (1938) The spectrum of turbulence. *Proceedings of the Royal Society of London. Series A-Mathematical and Physical Sciences*, **164**, 476–490.
- Tennekes, H. and Lumley, J. L. (1972) *A first course in turbulence*. MIT press.
- Tieleman, H. W. (1995) Universality of velocity spectra. *Journal of Wind Engineering and Industrial Aerodynamics*, **56**, 55–69.
- Tong, C. and Nguyen, K. X. (2015) Multipoint Monin–Obukhov similarity and its application to turbulence spectra in the convective atmospheric surface layer. *Journal of the Atmospheric Sciences*, **72**, 4337–4348.
- Verkaik, J. and Holtslag, A. (2007) Wind profiles, momentum fluxes and roughness lengths at cabauw revisited. *Boundary-Layer Meteorology*, **122**, 701–719.
- Villani, M., Schmid, H. P., Su, H.-B., Hutton, J. and Vogel, C. S. (2003) Turbulence statistics measurements in a northern hardwood forest. *Boundary-Layer Meteorology*, **108**, 343–364.
- Wilczek, M., Stevens, R. J. and Meneveau, C. (2015) Spatio-temporal spectra in the logarithmic layer of wall turbulence: large-eddy simulations and simple models. *Journal of Fluid Mechanics*, **769**, R1.
- Wyngaard, J. and Coté, O. (1974) The evolution of a convective planetary boundary layer – a higher-order-closure model study. *Boundary-Layer Meteorology*, **7**, 289–308.
- Wyngaard, J. C. (2010) *Turbulence in the Atmosphere*. Cambridge University Press.

GRAPHICAL ABSTRACT



Turbulence anisotropy has been shown to improve flux-variance and flux-gradient scaling, extending them to conditions where the assumptions of Monin-Obukhov similarity theory (MOST) are violated. Our work expands on these findings to spectral scaling in the unstable surface layer. Turbulence anisotropy, together with the stability parameter, is able to explain the low frequency spectral energy and the position of the spectral peak for velocity and temperature spectra. The novel spectral scaling elucidates on the nature of anisotropic eddies.